2D MXene–Molecular Hybrid Additive for High-Performance Ambipolar Polymer Field-Effect Transistors and Logic Gates

Hanlin Wang, Ye Wang, Zhenjie Ni, Nicholas Turetta, Sai Manoj Gali, Haijun Peng, Yifan Yao, Yusheng Chen, Iwona Janica, David Beljonne, et al.

DOI: 10.1002/((please add manuscript number))
Article type: Communication

2D MXene-Molecular Hybrid Additive for High-Performance Ambipolar Polymer Field-Effect Transistors and Logic Gates

*Hanlin Wang, Ye Wang, Zhenjie Ni, Nicholas Turetta, Sai Manoj Gali, Haijun Peng, Yifan Yao, Yusheng Chen, Iwona Janica, David Beljonne, Wenping Hu, Artur Ciesielski and Paolo Samorì**

Dr. H. Wang, Y. Wang, N. Turetta, H. Peng, Dr. Y. Yao, Y. Chen, Dr. A. Ciesielski and Prof. P. Samorì
Institut de Science et d'Ingénierie Supramoléculaires
University of Strasbourg & CNRS
8 allée Gaspard Monge
67000 Strasbourg, France.
E-mail: samori@unistra.fr

Dr. Z. Ni
School of Chemical Sciences
University of Chinese Academy of Sciences
Beijing 101408, P. R. China.

Dr. S. M. Gali, Prof. D. Beljonne
Laboratory for Chemistry of Novel Materials
University of Mons
Mons 7000, Belgium

Prof. W. Hu
Department of Chemistry
School of Science
Tianjin University
Tianjin, 300072, P. R. China

I. Janica, Dr. A. Ciesielski
Center for Advanced Technologies
Adam Mickiewicz University,
ul. Uniwersytetu Poznańskiego 10,
61614, Poznań, Poland

I. Janica,
Faculty of Chemistry,
Adam Mickiewicz University,
ul. Uniwersytetu Poznańskiego 8,
61614, Poznań, Poland

Keywords: MXene, intercalant, molecular additive, ambipolar polymer, organic field-effect transistors

Abstract:

MXenes are highly conductive layered materials that are attracting a great interest for high-performance opto-electronics and photonics applications as well as for energy storage and generation. Their non-covalent functionalization with *ad-hoc* molecules enables to produce stable inks of 2D flakes ready to be processed in thin-film electronics. Here, we demonstrate the formation of stable dispersions via the intercalation of $Ti_3C_2T_x$ with didecyldimethyl ammonium bromide (DDAB) yielding $Ti_3C_2T_x$-DDAB. Such functionalization modulates the properties of $Ti_3C_2T_x$, as evidenced by a 0.47 eV decrease of the work function as measured by photoelectron spectroscopy in air, corroborated by Density Functional Theory calculations. We also show that DDAB is a powerful *n*-dopant capable of enhancing electron mobility in conjugated polymers and 2D materials. When $Ti_3C_2T_x$-DDAB is blended with poly(diketopyrrolopyrrole-*co*-selenophene) [(PDPP-Se)], we observed a simultaneous increase by 170% and 152% of the hole and electron field-effect mobilities, respectively, compared to the neat conjugated polymer, with values reaching 2.0 $cm^2\ V^{-1}\ s^{-1}$. By exploiting the balanced ambipolar transport of the $Ti_3C_2T_x$-DDAB/PDPP-Se hybrid, complementary metal-oxide-semiconductor (CMOS) logic gates have been fabricated that displayed well-centered trip points and good noise margin (64.6% for inverter). Our results demonstrate that intercalant engineering represents an efficient strategy to tune the electronic property of $Ti_3C_2T_x$ yielding functionalized MXenes for polymer transistors with unprecedented performances and functions.

During the last decade, MXenes comprising transition metal carbides, nitrides and carbonitrides have been extensively investigated and tested for applications in energy storage, and electromagnetic interference shielding.[1-6] Because of their high conductivity reaching values of 11670 S cm^{-1},[7] remarkable surface area[8] and solution-processability (when non covalently functionalized),[9] MXenes appear ideal materials for applications in opto-electronics. Successful attempts have been made by employing MXenes both as electrodes and as active layers in field-effect transistors (FETs), light-emitting diodes (LEDs) and solar cells.[7,10-13] Their narrow bandgap render MXenes conductor thus yielding devices that cannot be switched-off.[14] However, blending MXenes with conjugated polymers makes it possible to generate bi-component films comprising conducting flakes connected by semiconducting polymers, the latter enabling efficient percolation pathways for fast charge transport within the active layer.[15] Such blending leads to organic field-effect transistors (OFETs) and photovoltaics with improved performances.[16,17]

Liquid phase exfoliation (LPE) and chemical exfoliation are effective and low-cost methods for mass production of 2D materials whose yield is enhanced via the use of specific solvent molecules[18] combined with butyl lithium[19] and organic ammonium salts as intercalants.[20] Cations from these ionic compounds functionalize the 2D material's surfaces thereby expanding the interlayer spacing when stacked.[21] Under external mechanical stimuli, such as sonication or shearing, the intercalated materials break apart into thin flakes.[22,23] Hence, intercalation makes it possible to modify the surface of 2D materials and increases interlayer-spacing and dispersity of the resulting flakes.[21,24] During the intercalation of layered materials with ammonium salts, the cationic (typically organic) species interact non-covalently with the surface of the 2D material. The scenario is therefore radically different compared to the chemical intercalation of 2D materials with alkali metal salts (e.g., butyl lithium), which affords aqueous dispersions of materials rich in charges, such as $Li^{+}(MoS_2)^{-}$. Therefore, the use of such alkali metal salt functionalized 2D flakes should be avoided when the 2D materials are

employed in electronics. Conversely, the use of ammonium salts guarantees negligible defect formation on the 2D material surface. Moreover, the remaining intercalating molecules change the chemical characteristics of 2D materials, e.g. via doping or defect passivation.[25-26] Such non-covalent functionalization of the intercalated flakes can allow to modulate the MXenes carrier density thus tuning their electronic properties. In particular, charge transport in few-layer materials is confined to 2D dimensions and hence it is markedly influenced by its local environment, like the presence of *ad hoc* chemical species such as intercalants. The properties of the synthetic intercalant can be programmed by chemical design, thus when the latter is added to MXenes, new properties can be conferred to the 2D materials.[27-29]

Blending 2D materials with semiconducting polymers represents an efficient strategy for improving the limited performances of organic polymer-based devices. In general, with their high conductivity and large surface-to-volume ratio, 2D materials embedded in polymer networks yield faster charge transport.[15,30] In addition, electronic properties (e.g., energy levels) in 2D materials can be tuned via control of their thickness, surface termination and non-covalent interactions with functional molecules. For example, MXenes such as 2D $Ti_3C_2T_x$ display a work function (WF) that is sensitive to their surface functionalization.[31] Furthermore, molecules intercalated or physisorbed on 2D $Ti_3C_2T_x$ affect the charge carrier type and charge density of semiconducting polymers. In particular, the counterions (halides and hydroxides) in ammonium intercalants can potentially *n*-dope organic semiconductors.[32] These factors thereby enhance the functional complexity to the hybrid made of intercalated 2D materials and semiconducting polymers. In this regard, the use of ammonium Lewis bases as intercalation compounds may offer new solutions for the generation of multicomponent materials and devices exhibiting unprecedented properties and performance.

Herein, we demonstrate that the intercalation of $Ti_3C_2T_x$ with a quaternary ammonium compound, i.e. didecyldimethyl ammonium bromide (DDAB), yields a remarkable increase of the charge carrier mobility in ambipolar polymer-based field-effect transistors (FETs).

Generally, conjugated polymers comprising an alternative donor-acceptor structure are expected to afford ambipolar transport or simultaneous *p*- and *n*-channel, thus enables complementary metal-oxide-semiconductor (CMOS) devices by one single material. We show DDAB serves as a bifunctional component, as it both promotes delamination of MXene through its intercalation and acts as *n*-dopant in blends used as active material in FETs. When $Ti_3C_2T_x$-DDAB is utilized as an additive, a simultaneous hole and electron transport improvement is observed in ambipolar polymer, poly(diketopyrrolopyrrole-co-selenophene) [(PDPP-Se)], as evidenced by an enhancement in averaged hole and electron mobility of 170% and 152% when compared to the neat PDPP-Se.

Among ambipolar polymers we have focused our attention to PDPP-Se and poly(isoindigo-*co*-bithiophene) [(PIID-BT)] because of their high hole mobility on the scale of 1.0 $cm^2\ V^{-1}\ s^{-1}$. Yet, their electron mobilities ($10^{-2} - 10^{-1}\ cm^2\ V^{-1}\ s^{-1}$) are comparably low.[33,34] Therefore, this feature renders them ideal platforms to assess the *n*-doping efficacy of the hybrid $Ti_3C_2T_x$-DDAB additive.

DDAB displays a specific design (**Figure 1**a) since it comprises alkyl ammoniums, which is beneficial for 2D material intercalation because of possible ion exchange via the replacement of the protons of the hydroxyl groups (Ti-OH) located on 2D $Ti_3C_2T_x$ sheet's surface with bulky quaternary ammonium (Figure 1b).[35] This, in turn, yields an increased interlayer spacing of 15.12 Å versus 9.95 Å in pristine $Ti_3C_2T_x$, as calculated from the (002) peaks in XRD (Figure S1, Supporting Information). The weakened interlayer interaction of $Ti_3C_2T_x$ makes it dispersible in solvents upon sonication. Moreover, the intercalated flakes are stabilized through Coulombic repulsions between ammonium ions attached to $Ti_3C_2T_x$. Besides their potential role as intercalant molecules, organic ammonium compounds, such as tetrabutylammonium hydroxide (TBAOH) and tetrabutylammonium fluoride (TBAF) are known to increase the electron transport in N2200-based FETs.[36] Zone-selective deposition of cetyltrimethyl ammonium bromide (CTAB) on a WSe_2 flake enables to realize a *p*-*n* homojunction,[37] where

anions from ammonium compounds induce electron transfer to the host semiconductors. In this research, bromide (Br^-) in DDAB is anticipated to act as a Lewis base to donate electrons to $Ti_3C_2T_x$ and PDPP-Se.

X-ray photoelectron spectroscopy (XPS) studies made it possible to gain insight into the chemical composition of DDAB-intercalated $Ti_3C_2T_x$. Figure 1c (upper panel) portrays the $Ti_3C_2T_x$-DDAB's Ti $2p_{3/2}$ and $2p_{1/2}$ spectra in the doublet form. Ti species are categorized into four groups according to their oxidation states. The peaks at 454.5 eV and 460.3 eV correspond to the Ti-C bond in $Ti_3C_2T_x$'s backbone. Signals at 455.8 eV and 462.1 eV are ascribed to Ti^{2+}, while peaks at 457.4 eV/463.6 eV can be attributed to Ti^{3+} species. Notably, TiO_2 signal appears at 458.6 eV/464.7 eV, evidencing the $Ti_3C_2T_x$'s instability under ambient oxidation. N 1s core level at 401.3 eV indicates the presence of DDAB nitrogen on $Ti_3C_2T_x$ surface (Figure 1c, bottom panel).

Photoelectron spectroscopy in air (PESA) made it possible to quantify $Ti_3C_2T_x$'s work function shift after DDAB treatment. While the work function of Ti_3C_2 was theoretically estimated as 4.22 eV (in absence of surface terminations), one can predict that oxygen and fluorine functionalization of $Ti_3C_2T_x$ surface yields an increase in its work function, whereas functionalization with hydroxyl groups leads to the opposite effect.[31] In Figure 1d, as-received $Ti_3C_2T_x$ displays a WF higher than Ti_3C_2, to reach 5.14 eV, due to its oxygen and fluorine surface terminations. After DDAB treatment, the WF of $Ti_3C_2T_x$ shifts downward to 4.67 eV regardless of oxygen and fluorine moieties (Figure S2, Supporting Information), thus indicating an electron transfer process from DDAB to $Ti_3C_2T_x$. Interestingly, HCl-LiF intercalated $Ti_3C_2T_x$ exhibits a similar WF of 4.60 eV.[12] Considering LiF's role as an *n*-dopant/electron injection layer in electronics,[38,39] the electron donation capability of fluoride is likely to be the origin of WF reduction. Density Functional Theory (DFT) calculations were performed to ascertain the work function of $Ti_3C_2T_x$, with and without DDAB intercalation, wherein the composition of T_x (containing oxygen, fluorine and hydroxyl groups) was proportionately

varied. As the percentage of hydroxyl/fluorine functionalization increases, a gradual decrease in work function is predicted (see Supplementary Information Tables S1 and S2). $Ti_3C_2T_x$ with a surface composition containing 81.25% of oxygen, 12.5% of hydroxyl and 6.25% of fluorine gives a theoretical work function of 5.20 eV, which decreases to 4.60 eV upon adsorption of DDAB, in good agreement with the experimental findings. This drop in work function originates from the combined effect of a partial charge transfer from DDAB to $Ti_3C_2T_x$ surface and a shift in electrostatic potential associated with the (axial component of) molecular dipole moment, as displayed in **Figure 2**. We further note that a similar *shift* in the work function due to DDAB adsorption is computed irrespective of the surface composition, though of course their *absolute* values vary (see Supplementary Information Figures S3 to S6 and Tables S1,2).

Scanning electron microscopy (SEM) imaging of the intercalated $Ti_3C_2T_x$-DDAB flakes revealed lateral sizes ranging from 400 nm to 2 μm (Figure 1g). The height of the flakes, as determined by atomic force microscopy (AFM), spans from 17 nm to 35 nm (Figure 1h). This average thickness is relatively larger than the one observed when using water as solvent;[14] such discrepancy can be ascribed to ethanol's inferior polarity consequently only partially hindering flake aggregation.[9]

Blend solutions of $Ti_3C_2T_x$-DDAB/PDPP-Se were prepared with a relative weight ratio ranging from 10^{-1} to 10^{-4}. Figure 1i displays a typical AFM phase image of the blend film (10^{-1} flake ratio) monitoring an area of 10 μm × 10 μm. The morphology of film samples and neat PDPP-Se are shown in Figure S7 (Supporting Information). With the decreasing flake weight ratio the sheet density of $Ti_3C_2T_x$ flakes decreases. The discontinuous $Ti_3C_2T_x$-DDAB film within 10 μm × 10 μm displays a root-square-mean roughness R_{RMS} = 9.07 nm, which is too high for being integrated in organic thin film device (Figure 1h). Fortunately, the amorphous PDPP-Se assembly forms a matrix surrounding the $Ti_3C_2T_x$-DDAB flakes efficiently smoothening the blend film (Figure S7l in the SI), thus enabling the fabrication of thin film devices.

To evaluate the ambipolar characteristics of these blend films, they were used as the active layer in a top-gate bottom-contact FET. Key parameters, including I_{on}/I_{off} ratio, field-effect mobility and onset voltage (V_{Onset}) are recorded for device assessment. **Figure 3**a,b display the typical transfer curves of $Ti_3C_2T_x$-DDAB/PDPP-Se (10^{-2} flake ratio) under negative and positive bias. The negative shift of V_{Onset} confirms an *n*-doping of $Ti_3C_2T_x$-DDAB to PDPP-Se. For the sake of comparison, a control experiment with neat PDPP-Se transistors is carried out. In Figure 3c, neat PDPP-Se shows an I_{on}/I_{off} ratio of 1,500~2,900 in both *p*- and *n*-channel. With the increased content of $Ti_3C_2T_x$-DDAB, the I_{on}/I_{off} ratio reduces monotonously to a minimum of 300~500 at 10^{-1}. Such a change can be ascribed to the increased gate leakage current determined by the film inhomogeneity caused by the presence of MXene and to the favoured charge transport through the conducting MXene percolation paths (Figure S8, Supporting Information).

With the increased content of $Ti_3C_2T_x$-DDAB, the electron mobility of the devices grows from an average of 0.67 $cm^2\ V^{-1}\ s^{-1}$ (for neat PDPP-Se) to 1.69 $cm^2\ V^{-1}\ s^{-1}$ (ratio, 10^{-2}). Meanwhile, a similar trend is observed for hole transport, whose mobility reaches an average value of 1.75 $cm^2\ V^{-1}\ s^{-1}$ at the ratio of 10^{-2} (Figure 3d,e). Upon further increase in the $Ti_3C_2T_x$-DDAB content (up to 10^{-1}) we observe a reduction of both hole and electron mobility (amounting to 1.11 and 1.16 $cm^2\ V^{-1}\ s^{-1}$), likely due to non-uniform nature of the film as a result of the flake aggregation. Typical transfer and output characteristics from each flake ratio are provided in Figure S9, Supporting Information. V_{Onset} is also found to depend on flake weight ratio (Figure 3f). Upon increasing the $Ti_3C_2T_x$-DDAB ratio, *n*-channel V_{Onset} decreases proportionally from 47 V (neat PDPP-Se) to a minimum of 39.4 V (10^{-1} flake ratio). In Figure S9, *p*-channel V_{Onset} upshifts from −36 V (neat PDPP-Se) to −41 V (10^{-1} flake ratio). This *n*-doping effect is likely due to bromide in $Ti_3C_2T_x$-DDAB that fills up the electron traps in PDPP-Se to enhance its electron density and transport, however, at the cost of enlarged *p*-channel V_{Onset}. Notwithstanding this limitation, the hole mobility displays a substantial improvement

similar to that of the electron. The maximum hole and electron mobility (~2.0 $cm^2\ V^{-1}\ s^{-1}$) can be simultaneously obtained at a ratio of 10^{-2}.

In view of the $Ti_3C_2T_x$-DDAB's complex surface terminations, device hysteresis upon back-and-forth sweeping was measured (Figure S10, Supporting Information). With a gate voltage (V_G) hold time of 0.05 s and delay time of 0.5 s, the transfer curve exhibits an anti-clockwise loop with ΔV_{Onset} of 3V, being 3.75% of the V_G applied (80 V) and slightly higher than that of 2V from pristine PDPP-Se.

All in all, the blend transistors display balanced ambipolar characteristics by well-centered V_{Onset} and acceptable hysteresis at the flake ratio of 10^{-2}.

To single out the doping effect from each component, we extended our electrical characterization to $Ti_3C_2T_x$-DDAB and DDAB/PDPP-Se based transistors. Under identical testing conditions, DDAB downshifts *n*-channel V_{Onset} more effectively than $Ti_3C_2T_x$-DDAB (Figure 3f). A low DDAB ratio of 10^{-4} produces a ΔV_{Onset} by −10 V. Further increase in DDAB ratio leads to V_{Onset} saturation, suggesting a limit for DDAB's electron trap-filling capability. Meanwhile, *p*-channel V_{Onset} upshifts by 5-7 V and the hole mobility remains nearly unchanged (Figure S11 and S12, Supporting Information). Therefore, DDAB is confirmed as an *n*-dopant for PDPP-Se. The maximum performance with averaged μ_h of 0.86 $cm^2\ V^{-1}\ s^{-1}$ and μ_e of 0.90 $cm^2\ V^{-1}\ s^{-1}$ was obtained under flake ratio of 10^{-3} (Figure S12, Supporting Information).

In view of the $Ti_3C_2T_x$-DDAB's attenuated *n*-doping effect against DDAB, we have studied MXene's role in blend transistors. One can postulate that fluorine atoms and oxidized Ti (Ti^{4+}) render $Ti_3C_2T_x$ an electron-accepting system, counterbalancing DDAB's *n*-doping effect. To verify this hypothesis, in Table 1, macroscopic Kelvin probe was employed to acquire the contact potential difference (V_{cpd}) between the film and the tip. V_{cpd} is defined by:

$$eV_{cpd} = \Phi_{sample} - \Phi_{tip} \quad (1)$$

with Φ_{sample} and Φ_{tip} being the work functions of the sample and the tip, e being the electronic charge. In Table 1, DDAB/PDPP-Se's V_{cpd} (−0.680 V) is deeper than that of $Ti_3C_2T_x$-

DDAB/PDPP-Se (−0.548 V), while $Ti_3C_2T_x$/PDPP-Se's V_{cpd} (0.006 V) notably exceeds that from neat PDPP-Se (−0.166 V). These data point to the opposite doping effect of $Ti_3C_2T_x$ against DDAB, which is in line with V_{Onset} difference displayed from respective transistors (Figure 3h), thus validating the aforementioned hypothesis.

To further study the spatially-resolved potential distribution in the blend film, Kelvin probe force microscopy (KPFM) was used. In $Ti_3C_2T_x$-DDAB/PDPP-Se, V_{cpd} (−0.193 V) is highly uniformly distributed without localized, abrupt potential changes (Figure S13a,d, Supporting Information). By comparison, neat PDPP-Se film presents a higher V_{cpd} of −0.033 V (Figure S13g,h, Supporting Information). In Figure S11b,e (V_{cpd}, −0.929 V), phase segregation induced DDAB clusters exhibit a higher potential than background, implying DDAB's electron-deficiency after electron transfer to PDPP-Se. In $Ti_3C_2T_x$/PDPP-Se (V_{cpd}, −0.064 V), $Ti_3C_2T_x$'s lower potential distribution implies higher electron-density than background (Figure S13c,f). Identical observation has been reported with a ZnO/P3HT blend.[40] The V_{cpd} sequence determines $Ti_3C_2T_x$/DDAB's inferior electron-donating capability versus DDAB and $Ti_3C_2T_x$ to be electron-withdrawing for PDPP-Se.

The concurrent improvement of hole and electron mobility in $Ti_3C_2T_x$-DDAB/PDPP-Se indicates the bi-functional nature of $Ti_3C_2T_x$-DDAB as suitable additive for simultaneous *p*- and *n*-doping of ambipolar polymers. As a proof-of-concept, a predominant *p*-type polymer, i.e. PIID-BT was investigated (Figure S14, Supporting Information). Compared with PDPP-Se, PIID-BT deeper HOMO (−5.19 eV) and higher LUMO (−3.60 eV) yield higher hole/electron injection barriers with gold. The $Ti_3C_2T_x$-DDAB/PIID-BT transistor characteristics in **Figure 4**a exhibits negatively shifted V_{Onset} and magnified drain current (I_{DS}) versus PIID-BT. Figure 4b plots the dependence of PIID-BT's *n*-channel V_{Onset} on $Ti_3C_2T_x$-DDAB content, which shifts from an average of 47 V to 39.8 V. At a flake ratio of 10^{-2}, a well-centered (41 V) V_{Onset} is observed, together with averaged hole/electron mobility approaching 0.21 $cm^2\ V^{-1}\ s^{-1}$ and 0.041 $cm^2\ V^{-1}\ s^{-1}$ (Figure 4c, d), respectively. On the same time, the I_{on}/I_{off} ratio from *p*- and *n*-

channel decreases by one order of magnitude when heavily doped (Figure S15, Supporting Information). By and large, $Ti_3C_2T_x$-DDAB represents an effective additive for PIID-BT transistors, regardless of PIID-BT slightly higher injection barrier with respect to PDPP-Se.

Conventional CMOS logic functions are developed by combining *p*- and *n*-type transistors. This can be simplified by using an ambipolar polymer as active material. In this framework, a major challenge is determined by the unbalanced ambipolar properties leading to CMOS with asymmetric transfer curves due to off-center trip points (the input voltage (V_{In}) point where output voltage (V_{Out}) equals V_{In}).

Because of its balanced ambipolar properties, $Ti_3C_2T_x$-DDAB/PDPP-Se (10^{-2} flake ratio) was chosen as channel material for CMOS. As an archetypical electronic component, an inverter was fabricated by two series-connected transistors with one common gate. Driven by a V_{DD} of 80 V, the inverter exhibits a trip point of 39.8 V, being quite close to $1/2V_{DD}$ (**Figure 5**a). The noise margin, which allows to quantify the inverter immunity to input voltage without triggering the switching,[41,42] is calculated to be 64.6% by the maximum square fitted within the transfer curve and its mirror. Differential processing of Figure 5a enables to quantify the gain, which reaches a maximum of 49.5 at V_{In} of 40 V (Figure 5b). The inverter's trip point is stable with a hysteresis window lower than 2 V upon back and forth sweeping (Figure 5c). To increase the functional complexity of the device, a NAND gate (NOT-AND) with 4 transistors was fabricated. In this device, a logic was followed that given two high input levels ('1' state), it can produce low logic or '0' state. Once either of its input terminals is biased with low level, logic high or '1' state is produced. As displayed in Figure 5d, as one input was biased with 80 V constantly and the other approached 40 V upon sweeping, a voltage inversion occurs at 39.3 V and 40.5 V. It should be noted that trip point here corresponds to $1/2V_{DD}$ (40 V), and it results from well-centered V_{Onset} and highly balanced ambipolar transport enabled in $Ti_3C_2T_x$-DDAB blended PDPP-Se.

In conclusion, we have demonstrated that the organic DDAB represents an efficient bifunctional component when combined with $Ti_3C_2T_x$ as it promotes the delamination of the MXene through its intercalation and acts as *n*-dopant. As an additive for OFETs, $Ti_3C_2T_x$-DDAB was found to markedly enhance PDPP-Se's hole and electron mobility with an improvement of 170% and 152%, respectively. Control experiments indicate that $Ti_3C_2T_x$-DDAB has a weaker *n*-doping efficiency compared to DDAB: in particular, Kelvin probe characterization reveals that $Ti_3C_2T_x$ counterbalancing DDAB *n*-doping efficiency, which results from fluorine terminations and Ti^{4+}'s electron-accepting capability. Consequently, the $Ti_3C_2T_x$-DDAB additive confers PDPP-Se balanced ambipolar properties, thereby allowing NOT and NAND gates with well-centered trip point and good noise margin. Our findings provide unambiguous evidence that $Ti_3C_2T_x$ surface electronic property can be tuned by intercalant chemistry and surface termination, which further alters the device characteristics by enhancing their functional complexity. Finally, the presented results and methodology provide an intercalant-engineering perspective for hybrid devices based on 2D materials and functional molecules.

Supporting Information
Supporting Information is available from the Wiley Online Library or from the author.

Acknowledgements
H.L.W. and Y.W. contributed equally to this work. We thank Dr. Marc-Antoine Stoeckel for enlightening discussions. This work was financially supported by the MX-OSMOPED project funded by the FLAG-ERA programme, the European Union and the Agence Nationale de la Recherche (ANR) (GA No. ANR-17-GRF1-0006-04), the EC Graphene Flagship Core 3 project (GA- 881603), the ANR through the Labex projects CSC (ANR-10-LABX-0026 CSC) and NIE (ANR-11-LABX-0058 NIE) within the Investissement d'Avenir program (ANR-10-120 IDEX-0002-02), the International Center for Frontier Research in Chemistry (icFRC) and the Chinese Scholarship Council. The work in Mons is supported by the Belgian National Fund for Scientific Research (FRS-FNRS), within FNRS-PDR-TOREADOR project (T.0051.18). Computational resources were provided by the Consortium des Équipements de Calcul Intensif (CÉCI) funded by F.R.S.-FNRS under Grant F.R.S.-FNRS under the conventions Nº 2.4.617.07.F and Nº 2.5020.11. DB is FNRS Research Director.

Received: ((will be filled in by the editorial staff))
Revised: ((will be filled in by the editorial staff))
Published online: ((will be filled in by the editorial staff))

Conflict of Interest

The authors declare no conflict of interest.

References

[1] B. Anasori, M. R. Lukatskaya and Y. Gogotsi, *Nat. Rev. Mater.* **2017**, *2*, 16098.

[2] Z. Ling, C. E. Ren, M.-Q. Zhao, J. Yang, J. M. Giammarco, J. Qiu, M. W. Barsoum, Y. Gogotsi, *Proc. Natl. Acad. Sci. USA* **2014**, *111*,16676.

[3] A. Sarycheva, A. Polemi, Y. Liu, K. Dandekar, B. Anasori, Y. Gogotsi, *Sci. Adv.* **2018**, *4*, eaau0920.

[4] J. Halim, M. R. Lukatskaya, K. M. Cook, J. Lu, C. R. Smith, L.-Å. Naslund, S. J. May, L. Hultman, Y. Gogotsi, P. Eklund, M. W. Barsoum, *Chem. Mater.* **2014**, *26*, 2374.

[5] K. Hantanasirisakul, Y. Gogotsi, *Adv. Mater.* **2018**, *30*, 1804779.

[6] F. Shahzad, M. Alhabeb, C. B. Hatter, B. Anasori, S. M. Hong, C. M. Koo, Y. Gogotsi, *Science* **2016**, *353*, 1137.

[7] S. Ahn, T.-H. Han, K. Maleski, J. Song, Y.-H. Kim, M.-H. Park, H. Zhou, S. Yoo, Y. Gogotsi, T.-W. Lee, *Adv. Mater.* **2020**, *32*, 2000919.

[8] W. Bao, X. Tang, X. Guo, S. Choi, C. Wang, Y. Gogotsi, G. Wang, *Joule* **2018**, *2*, 778.

[9] K. Maleski, V. N. Mochalin, Y. Gogotsi, *Chem. Mater.* **2017**, *29*, 1632.

[10] B. Xu , M. Zhu , W. Zhang , X. Zhen , Z. Pei, Q. Xue , C. Zhi, P. Shi, *Adv. Mater.* **2016**, *28*, 3333.

[11] J. Xu, J. Shim, J.-H. Park, S. Lee, *Adv. Funct. Mater.* **2016**, *26*, 5328.

[12] Z. Wang, H. Kim, H. N. Alshareef, *Adv. Mater.* **2018**, *30*, 1706656.

[13] A. Agresti, A. Pazniak, S. Pescetelli, A. Di Vito, D. Rossi, A. Pecchia, M. Auf der Maur, A. Liedl, R. Larciprete, D. V. Kuznetsov, D. Saranin, A. Di Carlo, *Nat. Mater.* **2019**, *18*, 1228.

[14] A. Lipatov, M. Alhabeb, M. R. Lukatskaya, A. Boson, Y. Gogotsi, A. Sinitskii, *Adv. Electron. Mater.* **2016**, *2*, 1600255.

[15] M. M Stylianakis, D. Konios, C. Petridis, G. Kakavelakis, E. Stratakis, E.Kymakis, *2D Mater.* **2017**, *4*, 042005.

[16] M. E. Gemayel, S. Haar, F. Liscio , A. Schlierf, G. Melinte, S. Milita, O. Ersen, A. Ciesielski, V. Palermo, P. Samorì, *Adv. Mater.* **2014**, *26*, 4814.

[17] G. Kakavelakis, A. E. Del Rio Castillo, V. Pellegrini, A. Ansaldo, P. Tzourmpakis, R. Brescia, M. Prato, E. Stratakis, E. Kymakis, F. Bonaccorso, *ACS Nano* **2017**, *11*, 3517.

[18] J. N. Coleman, M. Lotya, A. O'Neill, S. D. Bergin, P. J. King, U. Khan, K. Young, A. Gaucher, S. De, R. J. Smith, I. V. Shvets, S. K. Arora, G. Stanton, H. Y. Kim, K. Lee, G. T. Kim, G. S. Duesberg, T. Hallam, J. J. Boland, J. J. Wang, J. F. Donegan, J. C. Grunlan, G. Moriarty, A. Shmeliov, R. J. Nicholls, J. M. Perkins, E. M. Grieveson, K. Theuwissen, D. W. McComb, P. D. Nellist, V. Nicolosi, *Science* **2011**, *331*, 568.

[19] D. Yang, R. F. Frindt, *J. Phys. Chem. Solids* **1996**, *57*, 1113.

[20] Z. Lin, Y. Liu, U. Halim, M. Ding, Y. Liu, Y. Wang, C. Jia, P. Chen, X. Duan, C. Wang, F. Song, M. Li, C. Wan, Y. Huang, X. Duan, *Nature* **2018**, *562*, 254.

[21] J. Wan, S. D. Lacey, J. Dai, W. Bao, M. S. Fuhrer, L. Hu, *Chem. Soc. Rev.* **2016**, *45*, 6742.

[22] A. Ciesielski, P. Samorì, *Chem. Soc. Rev.* **2014**, *43*, 381.

[23] E. Varrla, C. Backes, K. R. Paton, A. Harvey, Z. Gholamvand, J. McCauley, J. N. Coleman, *Chem. Mater.* **2015**, *27*, 1129.

[24] K. Hantanasirisakul, M.-Q. Zhao, P. Urbankowski, J. Halim, B. Anasori, S. Kota, C. E. Ren, M. W. Barsoum, Y. Gogotsi, *Adv. Electron. Mater.* **2016**, *2*, 1600050.

[25] O. Mashtalir, M. R. Lukatskaya, M.-Q. Zhao, M. W. Barsoum, Y. Gogotsi, *Adv. Mater.* **2015**, *27*, 3501.

[26] Z. Lin, A. McCreary, N. Briggs, S. Subramanian, K. Zhang, Y. Sun, X. Li, N. J. Borys, H. Yuan, S. K. Fullerton-Shirey, A. Chernikov, H. Zhao, S. McDonnell, A. M. Lindenberg, K. Xiao, B. J. LeRoy, M. Drndić, J. C. M. Hwang, J. Park, M. Chhowalla, R. E. Schaak, A. Javey, M. C. Hersam, J. Robinson, M. Terrones, *2D Mater.* **2016**, *3*, 042001.

[27] D. Kiriya, M. Tosun, P. Zhao, J. S. Kang, A. Javey, *J. Am. Chem. Soc.* **2014**, *136*, 7853.

[28] M.-A. Stoeckel , M. Gobbi, T. Leydecker, Y. Wang, M. Eredia, S. Bonacchi, R. Verucchi, M. Timpel, M. V. Nardi, E. Orgiu, P. Samorì, *ACS Nano* **2019**, *13*, 11613.

[29] C. R. Ryder, J. D. Wood, S. A. Wells, Y. Yang, D. Jariwala, T. J. Marks, G. C. Schatz, M. C. Hersam, *Nat. Chem.* **2016**, *8*, 597.

[30] J. Huang, D. R. Hines, B. J. Jung, M. S. Bronsgeest, A. Tunnell, V. Ballarotto, H. E. Katz, M. S. Fuhrer, E. D. Williams, J. Cumings, *Org. Electron.* **2011**, *12*, 1471.

[31] Y.-X. Yu, *J. Phys. Chem. C* **2016**, *120*, 5288.

[32] C.-Z. Li, C.-C. Chueh, F. Ding, H.-L. Yip, P.-W. Liang, X. Li, A. K. Y. Jen, *Adv. Mater.* **2013**, *25*, 4425.

[33] H.-W. Lin, W.-Y. Lee, W.-C. Chen, *J. Mater. Chem.* **2012**, *22*, 2120.

[34] T. Lei, Y. Cao, Y. Fan, C.-J., Liu, S.-C. Yuan, J. Pei, *J. Am. Chem. Soc.* **2011**, *133*, 6099.

[35] M. Naguib, R. R. Unocic, B. L. Armstronga, J. Nanda, *Dalton Trans.* **2015**, *44*, 9353.

[36] J. Kim, D. Khim, K.-J. Baeg, W.-T. Park, S.-H. Lee, M. Kang, Y.-Y. Noh, D.-Y. Kim, *Adv. Funct. Mater.* **2016**, *26*, 7886.

[37] J. Sun, Y. Wang, S. Guo, B. Wan, L. Dong, Y. Gu, C.Song, C. Pan, Q. Zhang, L. Gu, F. Pan, J. Zhang, *Adv. Mater.* **2020**, *32*, 1906499.

[38] H. M. W. Khalil, M. F. Khan, J. Eom, H. Noh, *ACS Appl. Mater. Interfaces* **2015**, *7*, 23589.

[39] L. S. Hung, C. W. Tang, M. G. Mason, *Appl. Phys. Lett.* **1997**, *70*, 152.

[40] T. Xu, S. Venkatesan, D. Galipeau, Q. Qiao, *Sol. Energy Mater. Sol. Cells* **2013**, *108*, 246.

[41] J. Lohstroh, E. Seevinck, J. de Groot, *IEEE J. Solid-State Circuits* **1983**, *6*, 803.

[42] G. Gelinck, P. Heremans, K. Nomoto, T. D. Anthopoulos, *Adv. Mater.* **2010**, *22*, 3778.

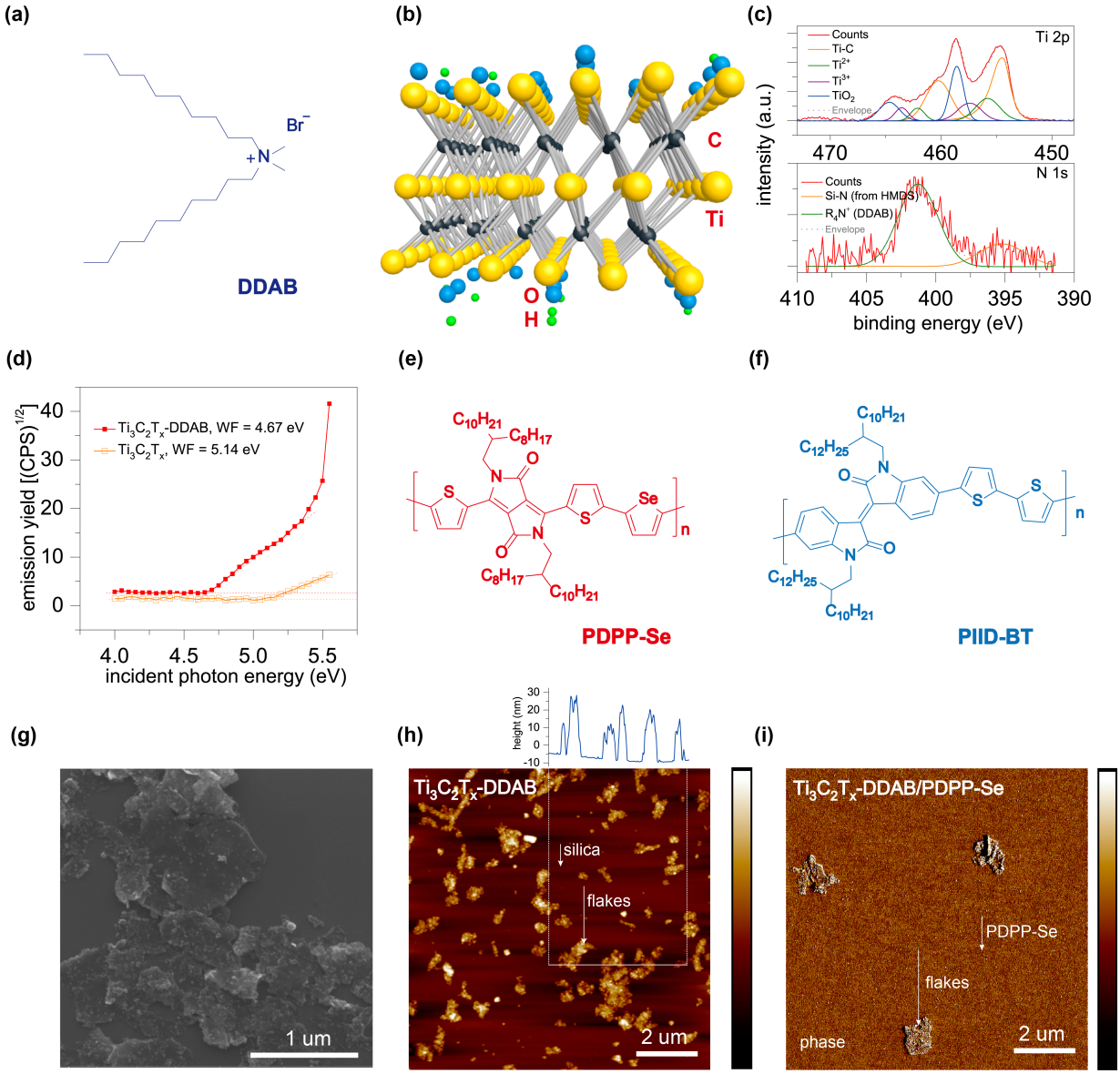

Figure 1. DDAB intercalated $Ti_3C_2T_x$ MXene and its surface properties. (a) Chemical structure of the intercalant, DDAB. (b) A 3D schematic illustration of a monolayer $Ti_3C_2T_x$ MXene. For the sake of clarity, fluorine atoms are not displayed. (c) Upper panel: X-ray photoelectron spectroscopy (XPS) spectra of Ti 2p. Bottom panel, XPS spectra of N 1s peak. The peak at 395.3 eV is ascribed to Si-N and it results from the hexamethyldisiloxane (HMDS) SAMs chemisorbed on SiO_2. This signal can serve as internal reference to distinguish ammonium nitrogen (401.3 eV). (d) Photoelectron spectroscopy in air measured work function for $Ti_3C_2T_x$-DDAB and unintercalated $Ti_3C_2T_x$. (e,f) Chemical structures of PDPP-Se and PIID-BT, respectively. (g) Scanning electron microscopy (SEM) image of DDAB intercalated $Ti_3C_2T_x$. (h) Atomic force microscopy (AFM) topography image of $Ti_3C_2T_x$-DDAB spin-coated film onto SiO_2. Z-scale = 80 nm. (i) AFM phase image of a blend of $Ti_3C_2T_x$-DDAB and PDPP-Se.

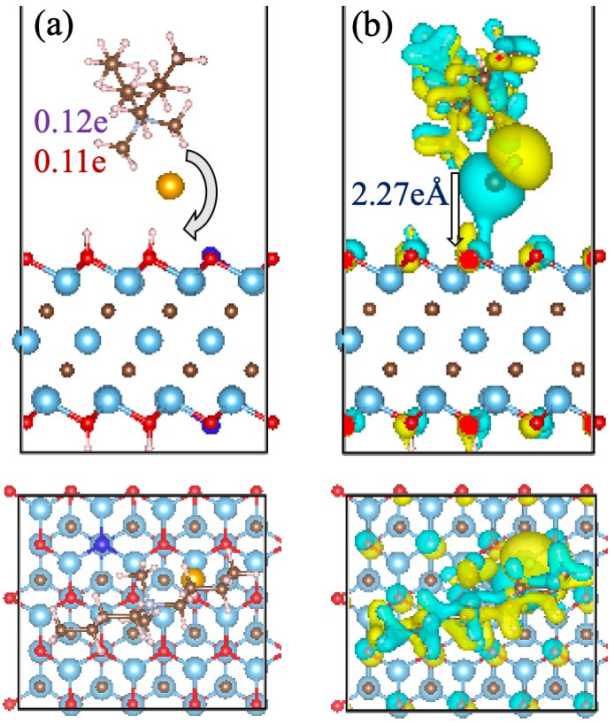

Figure 2. Optimized geometry of DDAB intercalated $Ti_3C_2T_x$ MXene. T_x was set to 81.25% O, 12.5% OH and 6.25% F. To limit the computational cost, DDAB molecules were simplified to two butyl (C4) linkers (dibutyl-dimethyl-ammonium bromide) instead of two decyl (C10) linkers connecting the central nitrogen atom. (a) The partial charge transfer (BADER in purple and DDEC6 in red) is shown both from side view (upper panel) and top view (bottom panel). (b) The axial component of dipole moment, directed towards the surface, along with the charge density (CD) difference plots (computed as $CD_{(Heterostructure)}-\{CD_{(surface)}+CD_{(Molecule)}\}$) are shown. For clarity: titanium, wathet; carbon, brown; oxygen, red; fluorine, blue; hydrogen, pink and bromide orange.

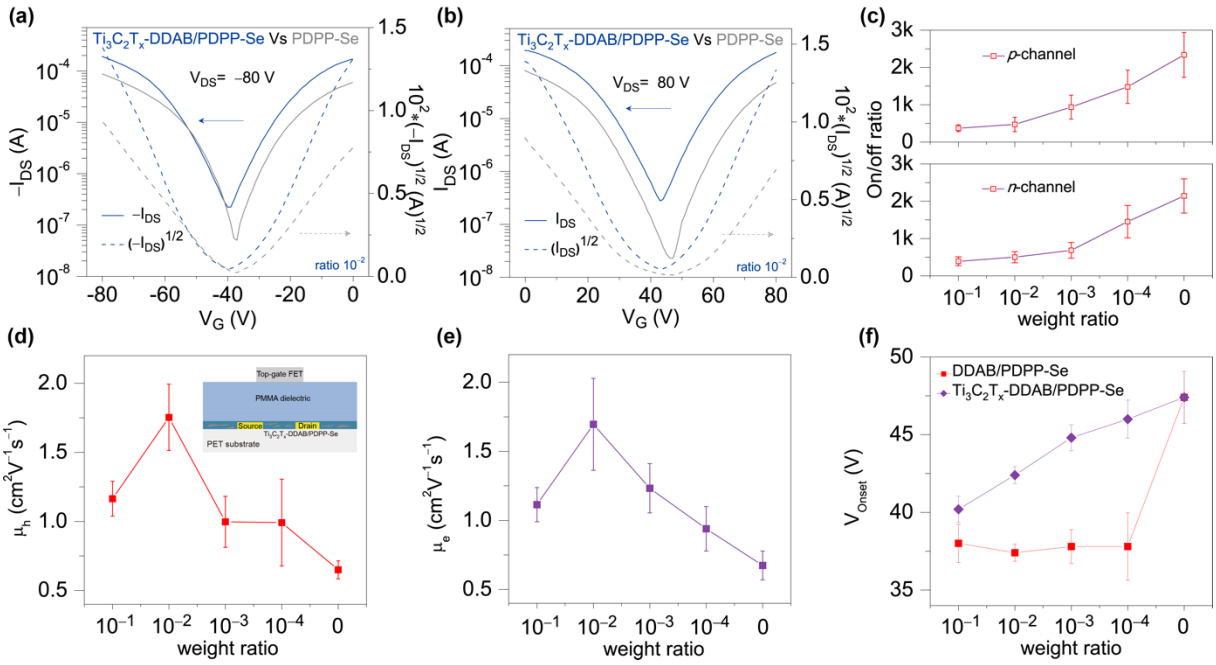

Figure 3. Electrical characterization of $Ti_3C_2T_x$-DDAB/PDPP-Se blend field-effect transistors. Ambipolar transfer curves of $Ti_3C_2T_x$-DDAB/PDPP-Se in (a) negative and (b) positive V_G region. For comparison, grey lines display (undoped) PDPP-Se curves. (c) Evolution of I_{on}/I_{off} ratio as a function of the content of $Ti_3C_2T_x$-DDAB as weight ratio. Upper panel, *p*-channel. Bottom panel, *n*-channel. $Ti_3C_2T_x$-DDAB/PDPP-Se's (d) hole (μ_h) and (e) electron mobility (μ_e) distribution versus $Ti_3C_2T_x$-DDAB weight ratio. Averaged values and standard deviation (s. d.) are calculated from at least 5 devices for each concentration (a total of 25 devices). Inset shows the device architecture used in this research. (f) A V_{Onset} control experiments. *N*-channel V_{Onset} of $Ti_3C_2T_x$-DDAB/PDPP-Se FETs and DDAB/PDPP-Se FETs are plotted as a function of additive weight ratio. It can be inferred that $Ti_3C_2T_x$-DDAB displays attenuated *n*-doping efficiency with respect to DDAB.

Table 1. Contact potential difference of film samples by macroscopic Kelvin probe (KP).

Film composition	DDAB/PDPP-Se	$Ti_3C_2T_x$-DDAB/PDPP-Se	(neat) PDPP-Se	$Ti_3C_2T_x$/PDPP-Se
Contact potential difference[a] (mV)	−680±91[b]	−548±48	−166±40	6±40

[a] Contact potential difference was measured by macroscopic Kelvin probe in the ambient. [b] Averaged value and standard deviation were calculated from three samples for each entry.

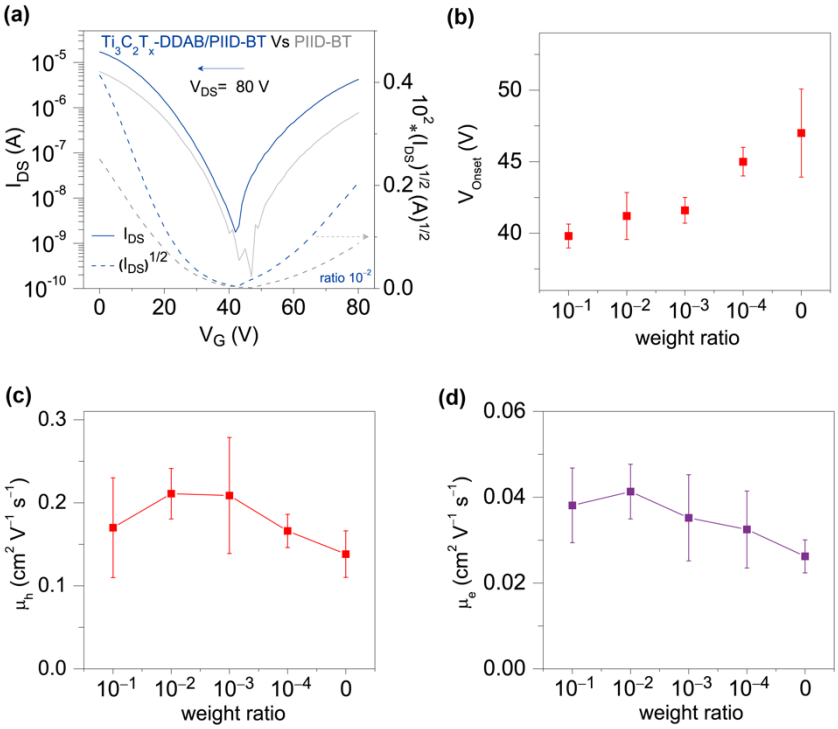

Figure 4. Device characterization of $Ti_3C_2T_x$-DDAB/PIID-BT blend FETs. (a) A typical $Ti_3C_2T_x$-DDAB/PIID-BT FET's transfer curve in the positive V_G region. $Ti_3C_2T_x$-DDAB weight ratio=10^{-2}. For comparison, a typical transfer curve from the neat PIID-BT FET is displayed. (b) $Ti_3C_2T_x$-DDAB/PIID-BT FETs' *n*-channel V_{Onset} as a function of $Ti_3C_2T_x$-DDAB (flake) weight ratio. Similar to PDPP-Se, PIID-BT FETs' *n*-channel V_{Onset} decreases with the increasing $Ti_3C_2T_x$-DDAB ratio. $Ti_3C_2T_x$-DDAB/PIID-BT's (c) hole and (d) electron mobility distribution versus $Ti_3C_2T_x$-DDAB weight ratio. Averaged values and standard deviation (s. d.) are calculated from at least 5 devices for each concentration (a total of 25 devices). The maximum averaged mobility is acquired at a flake ratio of 10^{-2}.

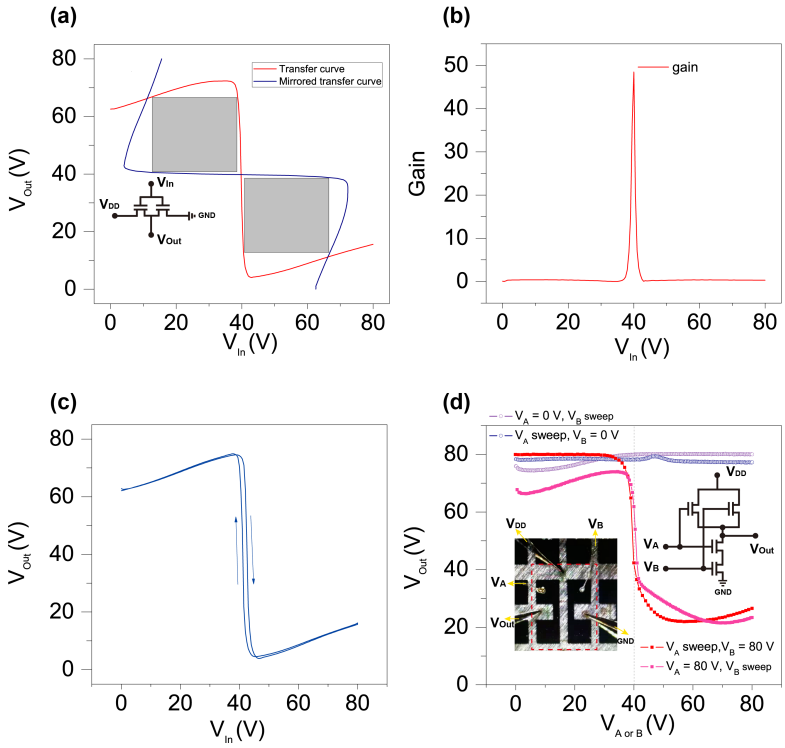

Figure 5. Simple CMOS logic gates based on $Ti_3C_2T_x$-DDAB/PDPP-Se blend FETs. Flake ratio = 10^{-2}. (a) Transfer curve and its mirror based on a $Ti_3C_2T_x$-DDAB/PDPP-Se inverter. (b) Differential of the inverter's transfer curve on V_{In} gives the gain. (c) Back and forth sweeping of the transfer curve yields a clockwise hysteresis window (ΔV_T is below 2V). (d) Typical V_{Out}-V_{In} transfer curve in a NAND gate made of 4 $Ti_3C_2T_x$-DDAB/PDPP-Se blend FETs. Due to the balanced ambipolar characteristics of $Ti_3C_2T_x$-DDAB/PDPP-Se (10^{-2}), voltage switching occurs approximately at 40 V. Inset shows a photograph of the NAND gate.